

## Using the Modified Nearest Neighbor Method to Correct Fiber-collision Effects on Galaxy Clustering

LEI YANG,<sup>1,2</sup> YIPENG JING,<sup>1,2,3</sup> XIAOHU YANG,<sup>1,2,3</sup> AND JIAXIN HAN<sup>1,4</sup>

<sup>1</sup>*Department of Astronomy, School of Physics and Astronomy, Shanghai Jiao Tong University  
Shanghai, 200240, China*

<sup>2</sup>*IFSA Collaborative Innovation Center, Shanghai Jiao Tong University  
Shanghai, 200240, China*

<sup>3</sup>*Tsung-Dao Lee Institute, Shanghai Jiao Tong University  
Shanghai, 200240, China*

<sup>4</sup>*Kavli IPMU (WPI), UTIAS, The University of Tokyo, Kashiwa, Chiba 277-8583, Japan*

(Accepted by ApJ)

### ABSTRACT

Fiber collision is a persistent problem faced by modern spectroscopic galaxy surveys. In this work, we propose a new method to correct for this undesired effect, focusing on the clustering from the fiber-collision scale up to  $\lesssim 10 \text{ Mpc } h^{-1}$ . We assume that the fiber-collided galaxies are in association with their nearest three angular neighbors. Compared with the conventional nearest-neighbor method, we have properly accounted for the foreground (background) galaxies that are associated with the foreground (background) cosmic webs relative to the nearest neighbor. We have tested the new method with mock catalogs of the Sloan Digital Sky Survey (SDSS) Data Release 7 (DR7). The test demonstrates that our new method can recover the projected two-point correlation functions at an accuracy better than 1% on small (below the fiber-collision scale) to intermediate (i.e.,  $10 \text{ Mpc } h^{-1}$ ) scales, where the fiber collision takes effect and the SDSS main sample can probe. The new method also gives a better recovery of the redshift-space correlation functions almost on all scales that we are interested in.

*Keywords:* cosmology: observation — cosmology: theory — galaxies: distance and redshifts — galaxies: halos — galaxies: statistics — large-scale structure of Universe

### 1. INTRODUCTION

The measurement of galaxy clustering plays a vital role in observational cosmology. As one of the most powerful probes of the growth rate of the matter density field, it can put strong constraints on the many fundamental quantities, including the cosmological parameters (Jing et al. 2002, 2006; Tegmark et al. 2006, 2004; Wang & Tegmark 2004; Yang et al. 2004; Seljak et al. 2005; Anderson et al. 2012; Sánchez et al. 2012, 2017; Cacciato et al. 2013; van den Bosch et al. 2013; Samushia et al. 2014; Shi et al. 2018), neutrino masses, the nature of gravity, and the properties of dark energy (Kaiser 1987; Peacock et al. 2001; Eisenstein et al. 2005; Guzzo et al. 2008; Reid et al.

2012; Contreras et al. 2013; Beutler et al. 2017; Wang et al. 2017). At the same time, galaxy clustering studies also provide crucial insights into the physics of galaxy formation and their connections to dark matter halos on small and intermediate scales (e.g., Springel et al. 2005; Croton et al. 2007; Dalal et al. 2008; Mo et al. 2010; Watson et al. 2010; Wang et al. 2013, 2018; Zentner et al. 2014; Piscionere et al. 2015; Yang et al. 2017).

To accurately measure galaxy clustering, fiber-fed spectroscopic galaxy surveys are generally required. However, these surveys often come with the inevitable problem of fiber collision (Gunn et al. 2006; Yoon et al. 2008; Dawson et al. 2013; Alam et al. 2015; Reid et al. 2016), which arises from the fact that two fibers cannot be placed closer than a separation limit called the fiber-collision scale. As a result, a small fraction of galaxies

in dense regions cannot be targeted for observation in these surveys.

For SDSS, the fiber-collision scale is  $55''$ , resulting in  $\sim 6\%$  of galaxies having no measured spectroscopic redshifts. The scale becomes slightly larger in the Baryon Oscillation Spectroscopic Survey (BOSS) (Anderson et al. 2012) and the Extended Baryon Oscillation Spectroscopic Survey (Dawson et al. 2016), which is  $62''$  and the population without redshift is  $\sim 5\%$ . The case for the Dark Energy Spectroscopic Instrument (DESI) (Levi et al. 2013; DESI Collaboration et al. 2016a,b) is more complicated compared with other surveys, which is dedicated to completing the largest spectroscopic survey with a 5000-fiber spectroscopic instrument. By simulating the fiber assignment algorithm, Pinol et al. (2017) found that only 49.5% of luminous red galaxies (LRGs) and 11.6% of the emission line galaxies (ELGs) can be observed for a one-pass survey in  $1 \text{ deg}^2$ , although the final expected achievements after multiple-pass observations for the full skies of LRGs and ELGs are 95% and 78%, respectively. Despite the fraction of fiber-collided galaxies being typically insignificant, its impacts on clustering are not trivial at all. Recent studies gradually demonstrate that it not only affects the precise clustering measurements below the fiber-collision scale, but also biases measurements on intermediate and larger scales (e.g., Zehavi et al. 2002, 2005; Guo et al. 2012). Furthermore, the multipoles of the power spectrum measured in redshift space can also be severely influenced by these effects (Hahn et al. 2017, hereafter Hahn17). Correcting for this fiber-collision problem is thus crucial for the application of galaxy clustering in the era of precision cosmology.

So far, various methods have been proposed to correct for fiber-collision effects. They can be basically divided into two categories. One category is to assign a redshift to each fiber-collided galaxy. For example, the nearest angular neighbor method simply assigns the redshift of the nearest neighbor to the fiber-collided galaxy (Zehavi et al. 2005, 2011; Berlind et al. 2006). Improved versions of this method are achieved by adding a distribution of the line-of-sight displacements between the fiber-collided galaxy and the nearest neighbor (Hahn17). The other category works by applying a weighting scheme to the pair counts in order to recover the true pair counts. The weights can be obtained from the angular correlation function (Hawkins et al. 2003; Li et al. 2006; White et al. 2011), the redshift completeness of the observed galaxies (Guo et al. 2012), the occurrence of close pairs (Anderson et al. 2012; Ross et al. 2012; Beutler et al. 2017; Gil-Marín et al. 2017), or the simulated selection function of the

pairs (Bianchi & Percival 2017; Bianchi et al. 2018). Both categories have their own advantages and disadvantages. For the first category, the redshift assignment methods, though widely used, are unable to recover the true clustering below the fiber-collision scale. For instance, the line-of-sight reconstruction method of Hahn17 successfully recovers the true power spectrum monopole on small scales compared with previous methods, but for the quadrupole power spectrum it shows little improvement. For the second category, the weighting algorithms generally require detailed tiling or spectroscopic mask information. These algorithms work very well in redshift space for high-completeness samples, but the correction to very low completeness samples may still show significant bias with large error bars. For example, by applying the method of Bianchi & Percival (2017) to the VIMOS Public Extragalactic Redshift Survey (Garilli et al. 2012) mock catalogs with only  $\sim 47\%$  completeness, Mohammad et al. (2018) found systematic underestimations of the multipole moments of the two-point correlation functions. Additionally, the weighting methods are also difficult to implement in Fourier space.

Instead of relying on the observational data to correct for the fiber-collision effects, Hahn17 proposed an alternative approach to recover the true power spectrum. By modeling the fiber-collision effects through a convolution of the true power spectrum with a scaled top-hat function, their effective window method can model the fiber-collided power spectrum down to the scale of  $k \approx 0.83h\text{Mpc}^{-1}$ , both in monopole and quadrupole. However, the effectiveness of this method for recovering the two-point correlation functions in real space is yet to be tested.

In this paper, we introduce a new redshift assignment method to correct for the fiber-collision effect below the fiber-collision scale and the intermediate scale  $\lesssim 10 \text{ Mpc } h^{-1}$ . The method falls into the first category, which can be used to measure clustering both in physical space and in Fourier space. We make an assumption that each fiber-collided galaxy is in association with its three nearest angular neighbors, and the coherence length for each galaxy pair is no more than  $20 \text{ Mpc } h^{-1}$  (Wang et al. 2011). We test our method with the two-point correlation statistics using mock catalogs. Compared with the previous methods, our method recovers galaxy clustering with smaller biases as well as smaller statistical errors on all scales.

The paper is organized as follows. We introduce the mock catalog construction in Section 2. We describe our new method in detail, including its statistical basis in Section 3. We present tests of the method and com-

pare with some other methods in Section 4. Finally, we summarize in Section 6.

## 2. CONSTRUCTION OF MOCK CATALOGS

We construct a mock galaxy catalog from a cosmological  $N$ -body simulation in the CosmicGrowth simulation suite (Jing 2018) WMAP\_3072\_600. This simulation is performed with a parallel adaptive P<sup>3</sup>M code adopting a standard flat  $\Lambda$ CDM cosmology. The parameters are set as  $\Omega_m = 1 - \Omega_\Lambda = 0.268$ ,  $\Omega_b = 0.045$ ,  $h = H_0/(100 \text{ km s}^{-1} \text{ Mpc}^{-1}) = 0.71$ ,  $\sigma_8 = 0.83$ , and  $n_s = 0.968$ , which are compatible with the observations of the Nine-Year *Wilkinson Microwave Anisotropy Probe* (WMAP 9; Bennett et al. 2013; Hinshaw et al. 2013). The simulation starts at an initial redshift of 144, and evolves with  $3072^3$  particles in a cubic box of  $600 \text{ Mpc } h^{-1}$  on a side, attaining a mass resolution of  $5.54 \times 10^8 M_\odot h^{-1}$ . There are 100 snapshots output evenly in the logarithm of the scale factor between  $z = 16.9$  and  $z = 0$ . The friends-of-friends algorithm (Davis et al. 1985) is applied to find halos in each snapshot with a linking length of 0.2 in units of the mean particle separation. Then, subhalos are identified together with their merger history using the Hierarchical Bound-Tracing code (Han et al. 2012, 2018). We include halos containing at least 50 particles in our halo catalog and pick the snapshot at  $z = 0$  for mock catalog construction.

We take into account the existence of “orphan” galaxies in our mock catalog. As a subhalo orbits within its host halo, its mass gradually decreases due to tidal stripping from its host. In some cases the mass of the subhalo can be stripped to below the resolution limit of our subhalo catalog, while the galaxy residing at the center of the subhalo can still survive unless the subhalo has merged with its host halo. Such a galaxy is called an “orphan” galaxy (Gao et al. 2004; Guo et al. 2011). To identify “orphan” galaxies, we keep tracking the most bound particle of each subhalo whose mass has been stripped to below our minimum mass cut. For each of these “orphan” subhalos, we then compute an infall time,  $t_{\text{infall}}$ , defined as the elapsed time from the epoch when the subhalo attains its peak mass during its evolution to the epoch of the analysis. We also estimate the expected time for the subhalo to merge into the center of its host halo,  $t_{\text{merge}}$ , according to the fitting function of Jiang et al. (2008) (their Equation (5)) with the factor  $C = 0.43$  and the orbital circularity  $\epsilon = 0.51$ . We keep all “orphan” subhalos satisfying  $t_{\text{merge}} > t_{\text{infall}}$  in our halo catalog as hosts of “orphan” galaxies.

We use the subhalo abundance matching technique (Kravtsov et al. 2004; Conroy et al. 2006; Vale & Ostriker 2006; Behroozi et al. 2010; Guo et al. 2010, 2016;

Simha et al. 2012; Guo & White 2014; Chaves-Montero et al. 2016; Wechsler & Tinker 2018) to link galaxies to their host dark matter subhalos. Specifically, each subhalo in our catalog is matched to a galaxy with a given luminosity assuming a monotonic relation between the galaxy absolute magnitude (or luminosity) and the peak mass of the subhalo,  $M_{\text{peak}}$ . Here,  $M_{\text{peak}}$  is the maximum mass that a subhalo ever had throughout its evolution history. We adopt the luminosity function of the SDSS DR7 “full1” sample as compiled from the New York University Value Added catalog (NYU-VAGC)<sup>1</sup> (Blanton et al. 2001, 2003, 2005) to perform the matching. The equation

$$n_g(> M_r^{0.1}) = n_{\text{subhalo}}(> M_{\text{peak}}) \quad (1)$$

is used to assign a galaxy magnitude,  $M_r^{0.1}$ , to a subhalo, where  $n_g$  and  $n_{\text{subhalo}}$  are the number densities of galaxies and subhalos, respectively. The galaxy is assumed to be located at the center of its assigned subhalo and inherits the position and velocity coordinates of the subhalo. We have not considered any scatter in the magnitude-mass correspondence  $n$  in our matching. Adding a scatter to the relation should affect the clustering of galaxies at the very luminous end. Since the aim of this work is to test our method of correcting for the fiber-collision effect, we believe adding the scatter should have little impact on our final test results. After this step, we duplicate the simulation box periodically to create a large box of mock galaxies. A random point within the box is then selected as the origin, and the galaxies are projected onto the celestial sphere to get their angular coordinates and true redshifts. We then derive the observed redshift of each galaxy, taking into account the peculiar velocity contribution, and the apparent magnitude,  $m_r$ , after  $k$ - and  $e$ -corrections. After that, the galaxy catalog is trimmed by the MANGLE software (Swanson et al. 2008) according to the survey mask of the SDSS “full1” sample, with angular and radial selection functions derived from NYU-VAGC. Finally, we use the fiber-collision code<sup>2</sup> of Guo et al. (2012) to add fiber-collision effects to the masked galaxy catalog. The fraction of fiber-collided galaxies in our final mock catalog perfectly matches the fraction  $\sim 5.6\%$  of the SDSS “full1” sample. By shifting the origin and rotating the box, we create a total of 33 mock catalogs for our following two-point statistical analysis. Figure 1 shows the normalized redshift distributions of the 33 mocks and that of the SDSS “full1” sample. The agreement

<sup>1</sup> <http://sdss.physics.nyu.edu/lss/dr72/>

<sup>2</sup> <http://sdss4.shao.ac.cn/guoh/>

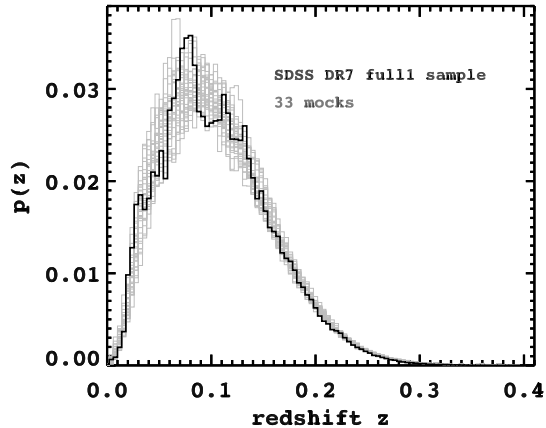


**Figure 1.** Normalized galaxy redshift distribution of the SDSS DR7 “full11” sample (black) and that of the 33 mock galaxy samples (gray).  $p(z)$  is the fraction of galaxies in each redshift bin, with a bin width of  $\Delta z = 0.004$ .

between the observed and the mock distributions is remarkably good.

### 3. THE NEW METHOD

In this section, we first analyze the statistical properties of galaxy pairs using the galaxy population without fiber collision. Then, based on these statistical properties, we elaborate our new approach to correct for the fiber-collision effects.

Our new method is developed on top of the nearest-neighbor method and the method of Hahn17. These previous methods make use of the distribution of the angular nearest neighbor to assign redshifts to fiber-collided galaxies. However, as we will see later, the nearest neighbor alone may not be sufficient to fully sample the redshift distribution of the fiber-collided galaxy. To improve over this, we also make use of the distribution of the second and third nearest neighbors in our redshift assignment scheme. Below we will present the statistical properties of these angular neighbors.

#### 3.1. Statistics of the Observed Galaxies

There are roughly 94.4% galaxies with well measured spectroscopic redshifts both in the SDSS DR7 “full11” sample and in our mock galaxy catalogs. A small fraction of galaxy pairs within the fiber-collision scale still have observed redshifts for both galaxies thanks to the overlapping tiling regions in the survey. Hahn17 measured the line-of-sight comoving distance separations of these close pairs with observed redshifts in BOSS DR12 CMASS. They found 70% of the galaxy pairs have  $|d_{\text{LOS}}| < 20 \text{ Mpc } h^{-1}$ , and the distribution of  $d_{\text{LOS}}$  can be roughly fitted by a Gaussian function within this distance range. The rest of the fiber-collided galaxy pairs,

**Table 1.** The Best-fitting Parameters for Pair Distributions

	$d_{\text{LOS}}^{01}$ ( $\text{Mpc } h^{-1}$ )	$d_{\text{LOS}}^{02}$	$d_{\text{LOS}}^{03}$
$\mu_1$ ( $\text{Mpc } h^{-1}$ )	-0.11	-0.10	-0.04
$\sigma_1$ ( $\text{Mpc } h^{-1}$ )	3.98	4.64	5.58
$A_1$ ( $\text{Mpc } h^{-1}$ )	0.07	0.06	0.05
$\mu_2$ ( $\text{Mpc } h^{-1}$ )	-0.10	-0.09	-0.02
$\sigma_2$ ( $\text{Mpc } h^{-1}$ )	1.39	1.47	1.81
$A_2$ ( $\text{Mpc } h^{-1}$ )	0.05	0.02	0.02
$B$	0.0002	0.0002	0.0002

NOTE—

The best-fitting functions return three parameters for individual Gaussian functions in equation (2) and a constant  $B$ . The three parameters are the mean  $\mu$ ,  $\sigma$ , and the area  $A$  of the best-fitting Gaussian curves.

showing a flat “tail” extending to  $\sim 500 \text{ Mpc } h^{-1}$ , follow a roughly uniform distribution. In our case, the fiber size of SDSS DR7 is  $55''$  and the median redshift of the “full11” sample is around  $\sim 0.1$ . These lead to a fiber-collision scale of  $0.1 \text{ Mpc } h^{-1}$ , which is smaller than the fiber-collided scale of BOSS. In this work, we collect all galaxy pairs with an angular separation satisfying  $\Delta\theta^{01} \leq 55''$  and treat one of them as a pseudo-fiber-collided galaxy “0.” We measure,  $d_{\text{LOS}}^{01} = |d_{\text{LOS}}^0 - d_{\text{LOS}}^1|$ , the line-of-sight comoving separation distance of the pseudo-fiber-collided galaxy “0” and its first angular nearest-neighbor galaxy “1” for all such galaxy pairs. Additionally, we also measure  $d_{\text{LOS}}^{02} = |d_{\text{LOS}}^0 - d_{\text{LOS}}^2|$  and  $d_{\text{LOS}}^{03} = |d_{\text{LOS}}^0 - d_{\text{LOS}}^3|$ , the line-of-sight separation of galaxy “0” and its second angular nearest-neighbor galaxy “2” and third angular nearest-neighbor galaxy “3.” Note these second and third nearest neighbors are not necessarily inside the fiber-collision scale from the pseudo-fiber-collided galaxy “0.” Figure 2 shows the normalized distributions of  $d_{\text{LOS}}^{01}$ ,  $d_{\text{LOS}}^{02}$ , and  $d_{\text{LOS}}^{03}$ , respectively. These distributions can all be well fit by sums of two Gaussian functions with different parameters (Markwardt 2009) as shown in Figure 2. The best-fitting values for our two Gaussian functions,

$$p(x) = \frac{A_1}{\sigma_1 \sqrt{2\pi}} e^{-\frac{(x-\mu_1)^2}{2\sigma_1^2}} + \frac{A_2}{\sigma_2 \sqrt{2\pi}} e^{-\frac{(x-\mu_2)^2}{2\sigma_2^2}} + B, \quad (2)$$

are presented in Table 1, where  $x$  refers to  $d_{\text{LOS}}^{01}$ ,  $d_{\text{LOS}}^{02}$ , or  $d_{\text{LOS}}^{03}$ .<sup>3</sup>

Table 2 presents the fractions of galaxy pairs with line-of-sight separations less than or equal to or larger than  $20 \text{ Mpc } h^{-1}$  in multiple conditions for the “full11”

<sup>3</sup> Here, we find that a single Gaussian function does not give a very good fit to the pair distributions

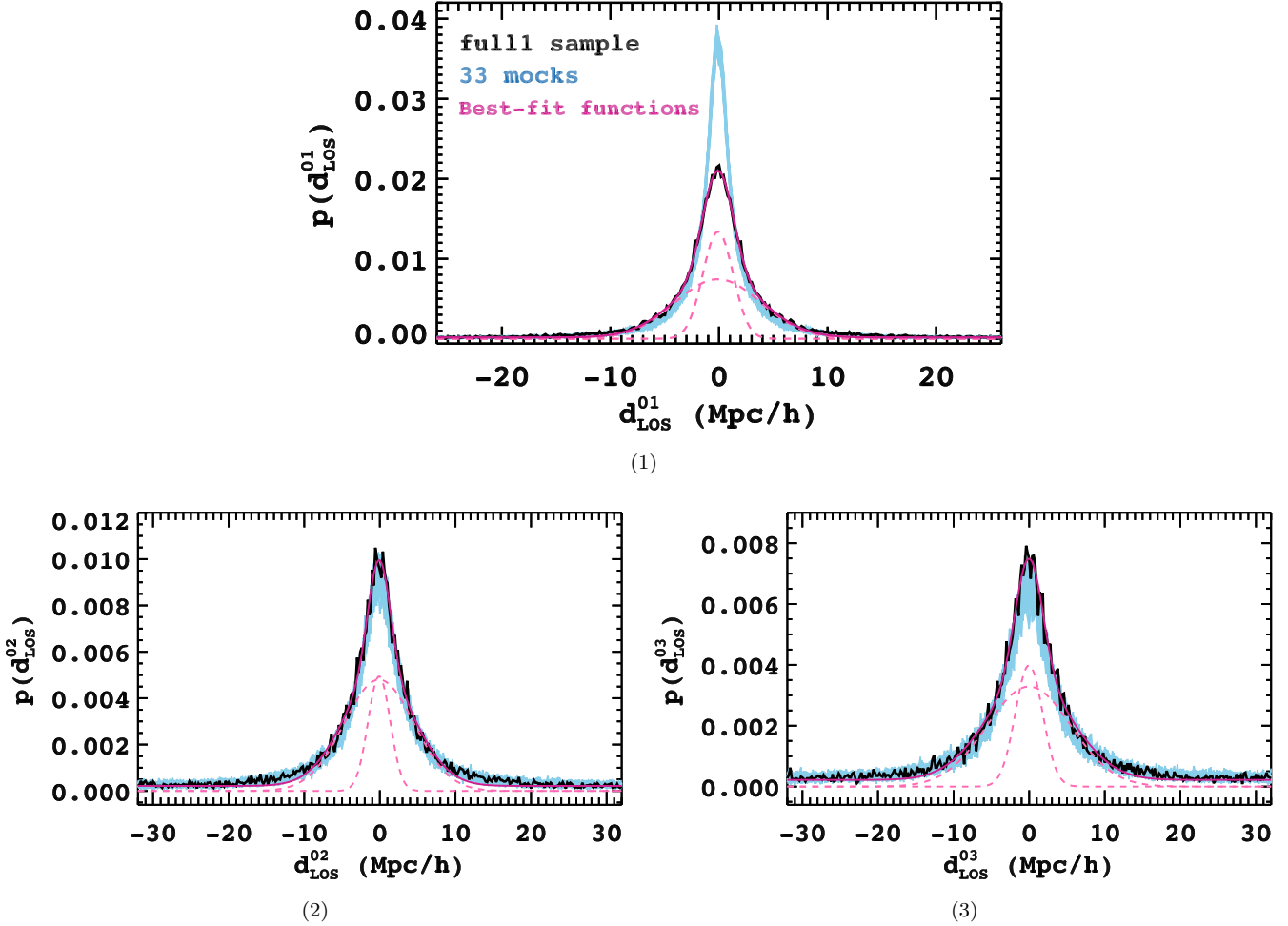


**Figure 2.** Normalized distribution of line-of-sight comoving separations between a candidate fiber-collided galaxy “0” and its angular neighbors. The three panels show the distribution of the separation to the galaxy’s nearest ( $d_{\text{LOS}}^{01}$ ), second nearest ( $d_{\text{LOS}}^{02}$ ), and third nearest neighbors ( $d_{\text{LOS}}^{03}$ ) respectively. The bin sizes,  $\Delta d = 0.2 \text{ Mpc } h^{-1}$ , are the same for different distributions. The black histograms are for the SDSS DR7 “full11” sample, while the blue histograms are distributions for the 33 mocks. The violet red curves show fits to the “full11” sample histogram, and the pink dashed curves show the two Gaussian components of each fit.

sample and 33 mocks. The superscript “0” denotes the central galaxy, and “1”, “2”, “3”, “4,” and “5” represent the first, second, third, fourth, and fifth nearest angular neighbors (from near to far) of the central galaxy, respectively.  $d_{\text{LOS}}$  is the line-of-sight comoving separation between these galaxy neighbor pairs. For  $d_{\text{LOS}}^{01}$ , we also require that the angular separation must be less than the angular scale of the fiber collision,  $\Delta\theta^{01} \leq 55''$ . From the table, we see that the fraction of pairs with  $d_{\text{LOS}} \leq 20 \text{ Mpc } h^{-1}$  rapidly decreases as it goes to the third neighbor, and only decreases slowly when it comes to the fourth and fifth neighbors. Although there are  $\sim 34\%$  of  $d_{\text{LOS}}^{04}$  and  $\sim 31.8\%$  of  $d_{\text{LOS}}^{05}$  galaxy pairs in the “full11” sample with  $d_{\text{LOS}}^{04,05} \leq 20 \text{ Mpc } h^{-1}$ , the fraction of their nearer-neighbor pairs satisfying  $d_{\text{LOS}}^{01,02,03} \leq 20 \text{ Mpc } h^{-1}$  simulta-

neously is extremely low, implying a very small probability that the fourth and the fifth neighbors are associated with the central galaxy “0” and other neighbors. The fraction distributions demonstrate that the third nearest neighbor of the central galaxy can be basically treated as a critical point when one tries to make a simple estimate on how many nearest neighbors are associated with the central galaxy. Furthermore, the fraction distributions of galaxy pairs can be imprinted in the clustering strength of galaxy correlation functions, particularly on small and intermediate scales. See Section 5 for a further description. Even on a large scale, galaxy pairs cannot be treated as random distributions because individual galaxies are settled in structures like filaments, sheets, or cosmic webs (Bond et al. 1996; Peebles 2001; Cautun et al. 2014). Therefore, in order to properly



**Table 2.** Statistics of galaxy pairs

$d_{\text{LOS}}$ ( $\text{Mpc } h^{-1}$ )	“full1” sample	33 Mocks
	Fraction <sup>(a)</sup>	Mean of fraction ( $1\sigma$ )
$ d_{\text{LOS}}^{01}  \leq 20$	66.2%	71.5%(0.40%)
$ d_{\text{LOS}}^{02}  \leq 20$	43.2%	40.4%(0.40%)
$ d_{\text{LOS}}^{03}  \leq 20$	37.5%	34.1%(0.35%)
$ d_{\text{LOS}}^{04}  \leq 20$	34.2%	30.9%(0.46%)
$ d_{\text{LOS}}^{05}  \leq 20$	31.8%	28.8%(0.50%)
$ d_{\text{LOS}}^{01}  \leq 20 \&  d_{\text{LOS}}^{02}  \leq 20$	34.4%	33.8%(0.41%)
$ d_{\text{LOS}}^{01}  \leq 20 \&  d_{\text{LOS}}^{02}  \leq 20 \&  d_{\text{LOS}}^{03}  \leq 20$	20.7%	18.7%(0.38%)
$ d_{\text{LOS}}^{01}  \leq 20 \&  d_{\text{LOS}}^{02}  \leq 20 \&  d_{\text{LOS}}^{03}  \leq 20 \&  d_{\text{LOS}}^{04}  \leq 20$	13.4%	11.4%(0.33%)
$ d_{\text{LOS}}^{01}  \leq 20 \&  d_{\text{LOS}}^{02}  \leq 20 \&  d_{\text{LOS}}^{03}  \leq 20 \&  d_{\text{LOS}}^{04}  \leq 20 \&  d_{\text{LOS}}^{05}  \leq 20$	9.2%	7.4%(0.30%)
$ d_{\text{LOS}}^{01}  > 20 \&  d_{\text{LOS}}^{02}  \leq 20$	8.9%	6.7%(0.14%)
$ d_{\text{LOS}}^{01}  > 20 \&  d_{\text{LOS}}^{02}  > 20 \&  d_{\text{LOS}}^{03}  \leq 20$	4.2%	3.3%(0.08%)
$ d_{\text{LOS}}^{01}  > 20 \&  d_{\text{LOS}}^{02}  > 20 \&  d_{\text{LOS}}^{03}  > 20 \&  d_{\text{LOS}}^{04}  \leq 20$	2.6%	2.2%(0.07%)
$ d_{\text{LOS}}^{01}  > 20 \&  d_{\text{LOS}}^{02}  > 20 \&  d_{\text{LOS}}^{03}  > 20 \&  d_{\text{LOS}}^{04}  > 20 \&  d_{\text{LOS}}^{05}  \leq 20$	1.9%	1.6%(0.06%)
$ d_{\text{LOS}}^{01}  \leq 20 \&  d_{\text{LOS}}^{02}  > 20$	31.8%	37.7%(0.44%)
$ d_{\text{LOS}}^{01}  \leq 20 \&  d_{\text{LOS}}^{02}  \leq 20 \&  d_{\text{LOS}}^{03}  > 20$	13.7%	15.1%(0.22%)
$ d_{\text{LOS}}^{01}  \leq 20 \&  d_{\text{LOS}}^{02}  \leq 20 \&  d_{\text{LOS}}^{03}  \leq 20 \&  d_{\text{LOS}}^{04}  > 20$	7.3%	7.3%(0.15%)
$ d_{\text{LOS}}^{01}  \leq 20 \&  d_{\text{LOS}}^{02}  \leq 20 \&  d_{\text{LOS}}^{03}  \leq 20 \&  d_{\text{LOS}}^{04}  \leq 20 \&  d_{\text{LOS}}^{05}  > 20$	4.1%	4.0%(0.18%)

NOTE—

$d_{\text{LOS}}^{01}$  denotes galaxy pairs with  $\Delta\theta^{01} \leq 55''$  in galaxy samples, where  $\Delta\theta^{01}$  is the angular separation between the fiber-collided galaxy “0” and its first nearest-neighbor galaxy “1” in the spherical coordinate;

(a) Fraction of galaxy pairs in total pairs that satisfy the corresponding condition. For example, there are 66.2% of  $d_{\text{LOS}}^{01}$  pairs in the “full1” sample have the comoving line-of-sight separations that are less than or equal to  $20 \text{ Mpc } h^{-1}$ , i.e.,  $|d_{\text{LOS}}^{01}| \leq 20 \text{ Mpc } h^{-1}$ ;

(b) “&” means multiple conditions are met at the same time.

recover the redshift distribution of fiber-collided galaxies and the pair distributions of angular neighborhood galaxies, these statistics should be carefully taken into account.

### 3.2. The Modified Nearest Neighbor Method

Based on the nearest angular neighbor method (hereafter, NN method; Berlind et al. 2006; Zehavi et al. 2011) that has been further developed by Hahn17, the new fiber-collision correction method we present in this paper is called the modified nearest angular neighbor method (MNN method). One key assumption of the MNN method is that the fiber-collided galaxies are tightly correlated with their three nearest angular neighbors.

First, using the statistical results derived from the galaxies with the well measured spectroscopic redshifts (see Section 3.1 for details), we construct three independent subsamples of galaxies:

- $\Phi^{01} = \{\mathbf{g} \mid \Delta\theta^{01} \leq 55''\}$ , where  $\mathbf{g}$  denotes galaxies.  $\Delta\theta^{01}$  is the angular separation between the central galaxy “0” and its first angular nearest-

neighbor galaxy “1.” Galaxy pairs in this subsample are selected to be within the fiber-collision scale,  $\Delta\theta^{01} \leq 55''$ , and with measured redshifts due to the overlapping tiling regions. Therefore, the line-of-sight comoving separation of this pair is available by  $d_{\text{LOS}}^{01} \equiv |d_{\text{LOS}}^0 - d_{\text{LOS}}^1|$ , where  $d_{\text{LOS}}^0$  and  $d_{\text{LOS}}^1$  denote the radial comoving distance of galaxy “0” and galaxy “1,” respectively.

- $\Phi^{02} = \{\mathbf{g} \mid d_{\text{LOS}}^{02} \leq 20 \text{ Mpc } h^{-1}\}$ . The second subsample is composed of galaxies “0” whose line-of-sight comoving separation to its second angular nearest-neighbor “2” satisfies  $d_{\text{LOS}}^{02} \leq 20 \text{ Mpc } h^{-1}$ . Here,  $d_{\text{LOS}}^{02} \equiv |d_{\text{LOS}}^0 - d_{\text{LOS}}^2|$ , where  $d_{\text{LOS}}^0$  and  $d_{\text{LOS}}^2$  denote the radial comoving distance of galaxy “0” and its second angular neighbor galaxy “2,” respectively.
- $\Phi^{03} = \{\mathbf{g} \mid d_{\text{LOS}}^{03} \leq 20 \text{ Mpc } h^{-1}\}$ . The third subsample consists of galaxies “0” whose line-of-sight comoving separation to its third angular nearest-neighbor “3” satisfies  $d_{\text{LOS}}^{03} \leq 20 \text{ Mpc } h^{-1}$ . Here,  $d_{\text{LOS}}^{03} \equiv |d_{\text{LOS}}^0 - d_{\text{LOS}}^3|$ , where  $d_{\text{LOS}}^0$  and  $d_{\text{LOS}}^3$  de-

note the radial comoving distance of galaxy “0” and its third angular neighbor “3,” respectively.

Note that galaxy “0” in  $\Phi^{01}$ ,  $\Phi^{02}$ , and  $\Phi^{03}$  may be different, depending on individual selection conditions. We also refer to galaxy “0” as the pseudo-fiber-collision galaxy, because some of these galaxies are below the fiber-collided scale but their redshifts are measured.

For the fiber-collided population, the comoving distance  $\tilde{d}_{\text{LOS}}^0$  of the fiber-collided galaxy is missing, but the redshifts of its angular neighbors have been well measured. For clarity, we use “ $\sim$ ” to denote the fiber-collision galaxies and their neighbors, distinguishing from the pseudo-fiber-collision galaxies. For each fiber-collided galaxy “ $\tilde{0}$ ,” we find the three angular nearest neighbors to the galaxy “ $\tilde{0}$ ” in the fiber-collision-free population. We label the three neighbors “ $\tilde{1}$ ,” “ $\tilde{2}$ ,” “ $\tilde{3}$ ” according to the size of the angular separation satisfying  $\Delta\theta^{01} \leq \Delta\theta^{02} \leq \Delta\theta^{03}$ . Because the neighbors are searched in the fiber-collision-free galaxies, the redshifts of these neighbors are also known. We use  $\tilde{d}_{\text{LOS}}^1$ ,  $\tilde{d}_{\text{LOS}}^2$ , and  $\tilde{d}_{\text{LOS}}^3$  to represent the comoving distance of the neighbor galaxies “ $\tilde{1}$ ,” “ $\tilde{2}$ ,” “ $\tilde{3}$ ,” respectively. The traditional nearest angular neighbor method sets  $\tilde{d}_{\text{LOS}}^0 = \tilde{d}_{\text{LOS}}^1$ , overestimating the correlation of galaxy “ $\tilde{0}$ ” and its nearest neighbor “ $\tilde{1}$ .” Hahn17 added a Gaussian distributed displacement  $d_{\text{LOS}}^{01}$  to the equation,  $\tilde{d}_{\text{LOS}}^0 = \tilde{d}_{\text{LOS}}^1 + d_{\text{LOS}}^{01}$ , corresponding to  $\sim 70\%$  fiber-collided galaxies in their CMASS sample, then they kept the remaining  $\sim 30\%$  galaxies as  $\tilde{d}_{\text{LOS}}^0 = \tilde{d}_{\text{LOS}}^1$ . This method alleviates the strong bias of the monopole power spectrum compared with the NN method, but there is still an obvious bias of the quadrupole power spectrum shown in their Figure 6.

Our MNN method is primarily developed based on the NN method and the method of Hahn17. Detailed steps are listed as follows:

1. We construct 11 bins of galaxy pairs according to the angular separations of the pairs, denoted by  $\Delta\theta_i$ , ranging from  $0''$  to  $55''$  with a step  $\delta\Delta\theta = 5''$ , where  $i = 1$  to 11. Both  $\Delta\theta^{01}$  of the fiber-collision-free population and  $\Delta\theta^{01}$  of the fiber-collided population fall into one of these bins.
2. For each galaxy “ $\tilde{0}$ ,” if  $\Delta\theta^{01}$  belongs to the  $j$ th bin  $\Delta\theta_j$ , we find galaxies “0” in the subsample  $\Phi^{01}$  with  $\Delta\theta^{01} \in \Delta\theta_j$ . Out of these galaxy “0”s we select 30 galaxies whose line-of-sight distances  $d_{\text{LOS}}^0$  are the closest to the distance  $\tilde{d}_{\text{LOS}}^1$  of galaxy “ $\tilde{1}$ .” After that, a galaxy is *randomly* selected from the 30 galaxies, then the  $d_{\text{LOS}}^{01}$  of this galaxy is set as  $\tilde{d}_{\text{LOS}}^{01} = d_{\text{LOS}}^{01}$ .

Finally, the new comoving distance for the fiber-collided galaxy “ $\tilde{0}$ ” is derived by  $\tilde{d}_{\text{LOS}}^0 = \tilde{d}_{\text{LOS}}^1 + \tilde{d}_{\text{LOS}}^{01}$ . If the new  $\tilde{d}_{\text{LOS}}^0$  falls out of the distance range of the whole sample  $[d_{\text{LOS}}^{\text{min}}, d_{\text{LOS}}^{\text{max}}]$ , we repeat the process of selecting one galaxy from  $N_{\text{near}}$  galaxies until a good  $\tilde{d}_{\text{LOS}}^0$  is obtained.

3. We keep  $\tilde{d}_{\text{LOS}}^0$  for the fiber-collided galaxy if  $\tilde{d}_{\text{LOS}}^0 \leq 20 \text{ Mpc } h^{-1}$ . Since  $\tilde{d}_{\text{LOS}}^0$  follows the distribution of  $d_{\text{LOS}}^{01}$ ,  $\sim 71\%$  of the fiber-collided galaxies will get an assigned distance,  $\tilde{d}_{\text{LOS}}^0$ . For the remaining 29% of galaxies, they are supposed to be located at a distance of at least  $20 \text{ Mpc } h^{-1}$  away from their nearest neighbor. So, we *randomly* select a galaxy from  $\Phi^{02}$  and set  $\tilde{d}_{\text{LOS}}^{0'} = \tilde{d}_{\text{LOS}}^2 + d_{\text{LOS}}^{02}$ . Note that we use the second nearest neighbor of galaxy “ $\tilde{0}$ ” instead of the first one.
4. We keep  $\tilde{d}_{\text{LOS}}^{0'}$  for the fiber-collided galaxy in step 3 if  $|\tilde{d}_{\text{LOS}}^{0'} - \tilde{d}_{\text{LOS}}^1| > 20 \text{ Mpc } h^{-1}$ . For the case of  $|\tilde{d}_{\text{LOS}}^{0'} - \tilde{d}_{\text{LOS}}^1| \leq 20 \text{ Mpc } h^{-1}$ , we *randomly* select a galaxy from  $\Phi^{03}$  and set  $\tilde{d}_{\text{LOS}}^0 = \tilde{d}_{\text{LOS}}^3 + d_{\text{LOS}}^{03}$ . Note that we use the third nearest neighbor here.

After the above steps, all fiber-collided galaxies are assigned new comoving distances. We highlight that selecting  $d_{\text{LOS}}^{01}$  on the basis of  $\Delta\theta$  bins is equivalent to appropriately adding the angular weight to the selection process, as neighbor pairs in the same angular bin should have similar angular correlation features. In step 2, different numbers of  $N_{\text{near}}$  would result in tiny changes of the clustering strength on small scales. We test this with  $N_{\text{near}} = 60, 100$  in Section 5.3, and both cases give negligible changes under the measurement errors. So, the choice of  $N_{\text{near}}$  has no significant effect on our clustering results. In steps 3 and 4, we assign galaxies with  $\tilde{d}_{\text{LOS}}^0 > 20 \text{ Mpc } h^{-1}$  to the position of their second neighbor (step 3) and third neighbor (step 4), naturally inheriting the intrinsic scatter of these pair distributions. In this way, these fiber-collided galaxies can be located in their second and third galaxy associations.

#### 4. TESTING THE NEW METHOD

In this section, we test the performance of the MNN method on recovering the projected two-point correlation functions (P2PCFs) and the multipole moments of correlation functions in redshift space using mock galaxy samples. In particular, we will compare the performance of our method with those of the NN method and the Hahn17 method.

##### 4.1. Clustering Estimators

Following the common way to calculate the correlation function (Huchra 1988; Hamilton 1992; Fisher et al. 1994), we define the redshift separation vector  $\mathbf{s} \equiv \mathbf{v}_1 - \mathbf{v}_2$  and the line-of-sight vector  $\mathbf{l} \equiv (\mathbf{v}_1 + \mathbf{v}_2)/2$ , where  $\mathbf{v}_1$  and  $\mathbf{v}_2$  are the redshift-space position vectors of a pair of galaxies. The separations parallel ( $\pi$ ) and perpendicular ( $r_p$ ) to the line of sight are derived as

$$\pi \equiv \frac{\mathbf{s} \cdot \mathbf{l}}{|\mathbf{l}|}, \quad r_p^2 \equiv \mathbf{s} \cdot \mathbf{s} - \pi^2, \quad (3)$$

and  $\mu = \pi/s = \cos\theta$ , where  $\theta$  is the angle between  $\mathbf{s}$  and  $\mathbf{l}$ . A grid of  $\pi$  and  $r_p$  is constructed by taking  $2 \text{ Mpc } h^{-1}$  as the bin size for  $\pi$  linearly up to  $60 \text{ Mpc } h^{-1}$  and 0.2 dex as the bin size for  $r_p$  logarithmically in the range of  $[0.01, 40] \text{ Mpc } h^{-1}$ . The estimator of Landy & Szalay (1993) is adopted as

$$\xi(r_p, \pi) = \frac{DD - 2DR + RR}{RR}, \quad (4)$$

where DD, DR, and RR are the numbers of data-data, data-random, and random-random pairs weighted by the angular completeness. By integrating  $\xi(r_p, \pi)$  along the line-of-sight separation  $\pi$  we derive the P2PCF (Davis & Peebles 1983),

$$w_p(r_p) \equiv 2 \int_0^\infty \xi(r_p, \pi) d\pi = 2 \int_0^{\pi_{max}} \xi(r_p, \pi) d\pi. \quad (5)$$

We also calculate the non-zero multipole moments  $\xi_0, \xi_2, \xi_4$  of the redshift-space 2PCF  $\xi(s, \mu)$ , because these quantities can be used to study the redshift distortion effects and put crucial constraints on cosmological parameters and dark energy models (Hamilton 1992; Peacock et al. 2001; Scoccimarro 2004; Eisenstein et al. 2005; Reid et al. 2012; Sánchez et al. 2012; de la Torre et al. 2013; Li et al. 2016). The multipole expansion of  $\xi(s, \mu)$  is (Hamilton 1992)

$$\xi(s, \mu) = \sum_i \xi_l(s) P_l(\mu), \quad (6)$$

where  $P_l$  is the  $l$ th order Legendre polynomial. The multipole moment  $\xi_l$  can be calculated as

$$\xi_l(s) = \frac{2l+1}{2} \int_{-1}^1 \xi(s, \mu) P_l(\mu) d\mu. \quad (7)$$

We use the bin size for  $s$  in the same way as for  $r_p$ , and  $\mu$  is cut into 20 bins with a linear step  $\Delta\mu = 0.1$  in the range of  $[-1, 1]$ . Generally, we use random points of 30 to 50 times the number of galaxies to reduce the shot noise. The KDTree code of Kennel (2004) is applied to accelerate the calculation of the pair counts.

## 4.2. Correlation Functions

In order to explore the influence of the fiber-collision effect on clustering for different luminous populations and to assess the performances of those different methods, we construct three volume-limited galaxy samples with different luminosity thresholds as shown in Table 3 (Guo et al. 2015). For the fiber-collided galaxies, after applying the MNN, NN, and the Hahn17 methods, we reestimate  $M_r^{0.1}$  with  $k$ - and  $e$ -corrections based on the new redshifts and apparent magnitudes. For the *true* redshifts and redshifts derived via the NN method and the Hahn17 method, we construct 33 mock samples for each luminosity bin. For the MNN method, in order to reduce the random noises caused by the random selection processes involved in the method (see Section 3.2 in bold letters), we repeat the MNN method 3 times for each mock, obtaining a total of 99 samples for each luminosity bin. Our main test results for  $w_p(r_p)$ ,  $\xi_0(s)$ ,  $\xi_2(s)$ , and  $\xi_4(s)$  are presented in Figures 3–6 accordingly.

The detailed estimations in the figures are presented as follows. The correlation functions shown in the upper panels are derived as

$$\bar{X} = \frac{\sum_{i=1}^{N_{\text{mocks}}} X_i}{N_{\text{mocks}}}, \quad (8)$$

where  $X_i$  can be  $w_p(r_p)$ ,  $\xi_0(s)$ ,  $\xi_2(s)$ , and  $\xi_4(s)$ , and  $i$  is the  $i$ th mock. For  $X_{\text{true}}$ ,  $X_{\text{NN}}$ , and  $X_{\text{Hahn17}}$ ,  $N_{\text{mocks}} = 33$ . For  $X_{\text{MNN}}$ ,  $N_{\text{mocks}} = 99$ . Error bars are the  $1\sigma$  variations of  $X$  computed as

$$\sigma = \sqrt{\frac{1}{N_{\text{mocks}} - 1} \sum_{i=1}^{N_{\text{mocks}}} (X_i - \bar{X})^2}. \quad (9)$$

The lower panels in Figure 3 through Figure 6 show the mean ratios  $\bar{r}_X$  of the correlation functions. First, we define

$$r_{i,X} = \frac{X_i(\text{MNN/NN/Hahn})}{X_i(\text{true})}, \quad (10)$$

where  $X_i$  is the same as in equation (8). Then, the mean ratios are calculated as

$$\bar{r}_X = \frac{\sum_{i=1}^{N_{\text{mocks}}} r_{i,X}}{N_{\text{mocks}}}. \quad (11)$$

The error bars in the lower panels are estimated as

$$\bar{\sigma}_r = \sqrt{\frac{1}{N_{\text{mocks}} - 1} \sum_{i=1}^{N_{\text{mocks}}} (r_{i,X} - \bar{r}_X)^2}, \quad (12)$$

where  $N_{\text{mocks}}$  in equation (11) and (12) are the same as in equation (8).



**Table 3.** Galaxy samples

$M_r^{0.1}$	$z_{\min}$	$z_{\max}$	$N_{\text{true}}$	$N_{\text{MNN}}$	$N_{\text{NN}}$	$N_{\text{Hahn}}$
$\leq -19$	0.02	0.064	78898(5988)	78296(5889)	78373(5957)	78372(5957)
$\leq -20$	0.02	0.106	134479(5645)	133853(5545)	134040(5624)	134039(5625)
$\leq -21$	0.02	0.159	77382(1446)	77718(1444)	77821(1453)	77820(1454)

NOTE—Samples are constructed using galaxies with  $\text{fgot} \geq 0.5$  and  $m_r \leq 17.77$ . Galaxies are cut into three luminosity bins with different redshift ranges.  $N$  is the mean number of luminosity bins, and the numbers in brackets are  $1\sigma$  variation among the samples. For *true*, the MNN method, the NN method, and the [Hahn17](#) method, 33 mocks are used.

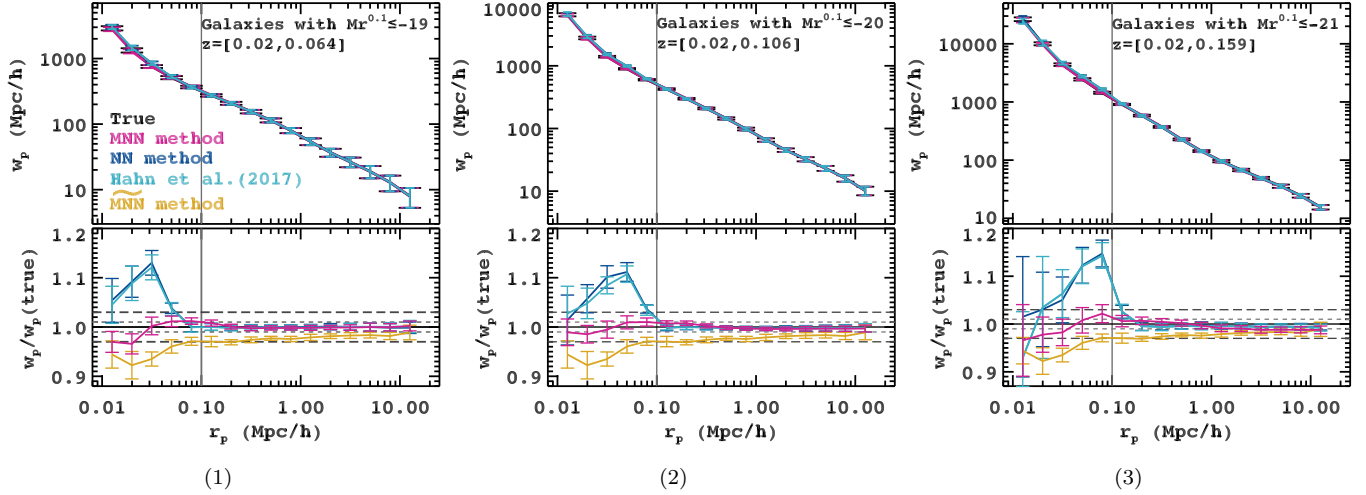


**Figure 3.** Comparisons of the projected two-point correlation functions  $w_p(r_p)$  estimated from different fiber collision correction methods for volume-limited galaxy samples within three luminosity thresholds. In the upper panels, the redshifts of the fiber-collided galaxies are from the *true* redshifts (black), redshifts generated from the MNN method (magenta), the NN method (dark blue), and the [Hahn17](#) method (light blue), separately. Every  $w_p(r_p)$  as shown in figures is the mean value of 33 mock samples for  $w_p(\text{true})$ ,  $w_p(\text{NN})$ , and  $w_p(\text{Hahn})$  method, and 99 mock samples for  $w_p(\text{MNN})$ . Error bars of  $w_p(r_p)$  are  $1\sigma$  variations of  $w_p(r_p)$  among the samples. In the lower panels, the mean ratios of  $w_p(r_p)$  estimated from different methods are presented, i.e.,  $w_p(\text{MNN})/w_p(\text{true})$  (magenta),  $w_p(\text{NN})/w_p(\text{true})$  (dark blue),  $w_p(\text{Hahn})/w_p(\text{true})$  (light blue), and  $w_p(\widetilde{\text{MNN}})/w_p(\text{true})$  (yellow). To highlight the importance of introducing the second and third neighbors on fiber-collision corrections, we measure  $w_p(\widetilde{\text{MNN}})$  by just executing the first two steps of the MNN method. In this case 29% of galaxy pairs are separated at  $d_{\text{LOS}}^{01} > 20 \text{Mpc } h^{-1}$  following step 2 with no further optimizations of the pair distributions. The error bars for ratios are the  $1\sigma$  variation among the ratios of all samples belonging to the same volume-limited luminosity bin. For clarity, we also mark the 1% (horizontal short dashed gray lines) and 3% (horizontal dashed gray lines) bias levels in lower panels. The vertical straight gray lines denote the fiber-collision scale.

#### 4.2.1. The Projected Two-point Correlation Functions

Figure 3 shows the P2PCFs estimated with different methods for three volume-limited mock galaxy samples. We also measure the true P2PCF for each sample using the true redshifts of the fiber-collided galaxies. The ratios between  $w_p$  and  $w_p(\text{true})$  are presented in the lower panels. To stress the essential roles of introducing the second and the third angular neighbor galaxies in the redshift reconstruction, we further measure the  $w_p(\widetilde{\text{MNN}})$  and derive the ratio of  $w_p(\widetilde{\text{MNN}})/w_p(\text{true})$  as shown in the yellow curves in the lower panels. In the  $\widetilde{\text{MNN}}$  method, we remove the step 3 and step 4 of

the MNN method, which means only the subsample  $\Phi^{01}$  is used in the redshift recovery process,<sup>4</sup> resulting in 29% fiber-collided galaxies having  $d_{\text{LOS}}^{01} > 20 \text{Mpc } h^{-1}$ . It also implies that about 29% of the fiber-collided galaxies are *randomly* distributed in the foreground or background. Although the final distributions of  $d_{\text{LOS}}^{01}$  for the fiber-collided galaxies totally trace the pair distribution  $d_{\text{LOS}}^{01}$  of the fiber-collision-free galaxies with known redshifts, our key assumption of the MNN method is

<sup>4</sup> The  $\widetilde{\text{MNN}}$  method is still different from the [Hahn17](#) method.

not adopted in the  $\widetilde{\text{MNN}}$  method. As a result, it leads to obvious declinations below the fiber-collision scale in  $w_p(\widetilde{\text{MNN}})$  for all three cases as shown in the figures, and these underestimations also extend to the intermediate scale and even the large scale, producing a  $\sim 3\%$  bias. Compared with the previous two methods and the  $\widetilde{\text{MNN}}$  method, the P2PCFs estimated from the MNN method give the best agreement with  $w_p(\text{true})$  on all concerned scales in all three luminosity samples. By further accounting for the pair distributions of  $d_{\text{LOS}}^{02}$  and  $d_{\text{LOS}}^{03}$ , our MNN method successfully reduces the bias to  $\sim 1\%$  on all scales. The underestimation of  $w_p$  by the  $\widetilde{\text{MNN}}$  method on large scales is also corrected by the MNN method properly. However, there is a weak luminosity dependence of the correction that can be seen in the figures. Specifically, the MNN method tends to work better for faint samples. For the brightest galaxy samples, the correction on  $\lesssim 1 \text{ Mpc } h^{-1}$  scales is only slightly better than the  $\widetilde{\text{MNN}}$  method, given the larger error bars. We also note that there is a very small ( $< 1\%$ ) deficiency in  $w_p(\text{MNN})$  on large scales, indicating that these massive galaxies might have more compact distributions around their nearest angular neighbors.

#### 4.2.2. The Redshift-space Correlation Functions

The non-zero multipole moments of the redshift-space correlation functions  $\xi(s, \mu)$  are presented in Figure 4 for  $\xi_0(s)$ , Figure 5 for  $\xi_2(s)$ , and Figure 6 for  $\xi_4(s)$ . The symbols and colors are the same as those in Figure 3 for the P2PCFs. Below the fiber-collision scale, the MNN method apparently provides a better correction compared with other methods. The  $\xi_0(s)$ s estimated from the NN method and the Hahn17 method exhibit significant deviations from the true values, while that from the MNN method agrees with the true  $\xi_0(s)$  within the  $1\sigma$  error. On scales between 0.1 and 1.0  $\text{Mpc } h^{-1}$ , we see significant deviations from the true  $\xi_0(s)$  in the NN method, while the deviations in the MNN and the Hahn17 methods are quite small. Although the MNN method gives a better recovery of the true  $\xi_0(s)$ , we note that there is an underestimation of  $3\% \sim 10\%$  beyond the fiber-collision scale and extending to  $\sim 2.0 \text{ Mpc } h^{-1}$ . The underestimations can also be seen in  $\xi_2(s)$ ,  $\xi_4(s)$ , but is absent in  $w_p$ . A simple explanation is that these underestimations are mainly caused by the linear coherent motion, or the peculiar velocities of galaxies. The influence of peculiar velocities on galaxy clustering has been well averaged out through the line-of-sight integration for the projected two-point correlation functions. In the case of the redshift space correlation functions, however, the galaxy peculiar velocities play a crucial role on the small scales, especially on the one-halo scale. There-

fore, in all of the fiber-collision correction methods, the effects of the peculiar velocities should be further corrected in the ideal case.

Figure 5 and Figure 6 show the redshift-space correlation functions  $\xi_2(s)$  and  $\xi_4(s)$ . The overall performances of the different fiber-collision correction methods for these measurements are quite similar to those for  $\xi_0(s)$ , except that the reduction seen on intermediate scales in  $\xi_0(s)$  is not prominent at all in the recovery of  $\xi_2(s)$  and  $\xi_4(s)$ .

## 5. DISCUSSIONS

### 5.1. Limitations of the MNN Method

Although the MNN method produces the best results around the fiber-collision scale, its application strongly relies on the availability of the collision-free galaxies with measured redshifts within the fiber-collision scale. These collision-free galaxies are normally only available for surveys with overlapping tiling regions. Moreover, the existence of biases indicates that there is still room to further improve the MNN method.

The key assumption of the MNN method is that every fiber-collided galaxy is assumed to be in association with its three nearest angular neighbors, i.e., they reside in the same large-scale environment. This assumption guarantees that not only the distribution of  $\widetilde{d}_{\text{LOS}}^{01}$  follows the distribution of  $d_{\text{LOS}}^{01}$  derived from galaxies with measured redshifts, but  $\widetilde{d}_{\text{LOS}}^{02}$  and  $\widetilde{d}_{\text{LOS}}^{03}$  also approximately trace the distribution of  $d_{\text{LOS}}^{02}$  and  $d_{\text{LOS}}^{03}$ . This assumption has a solid strong statistical basis as shown in Table 2 and Figure 2, which are derived from both the observational data and the corresponding mocks. The basis also tightly depends on a precondition, that there must be galaxies with measured redshifts below the fiber-collision scale. Actually, it is not too difficult to achieve this precondition. For a single-pass survey, there are often some overlapping tiling regions that enable some galaxy pairs within the fiber-collision scale to be both observed, while multi-pass surveys can provide plenty of these kinds of galaxies. With more galaxies observed spectroscopically below the fiber-collision scale, the pair distributions are closer to the real distributions, and the clustering measured by applying the MNN method becomes more reliable and robust. This argument works for any methods that are trying to correct the missing redshifts in two-point statistics.

The results of the MNN method exhibit a slight luminosity dependence, particularly the faint samples show a better correction below the fiber-collision scale than the luminous samples. This trend could be explained by the assumption of the MNN method as mentioned before. Fiber collisions mainly happen in galaxy-dense regions

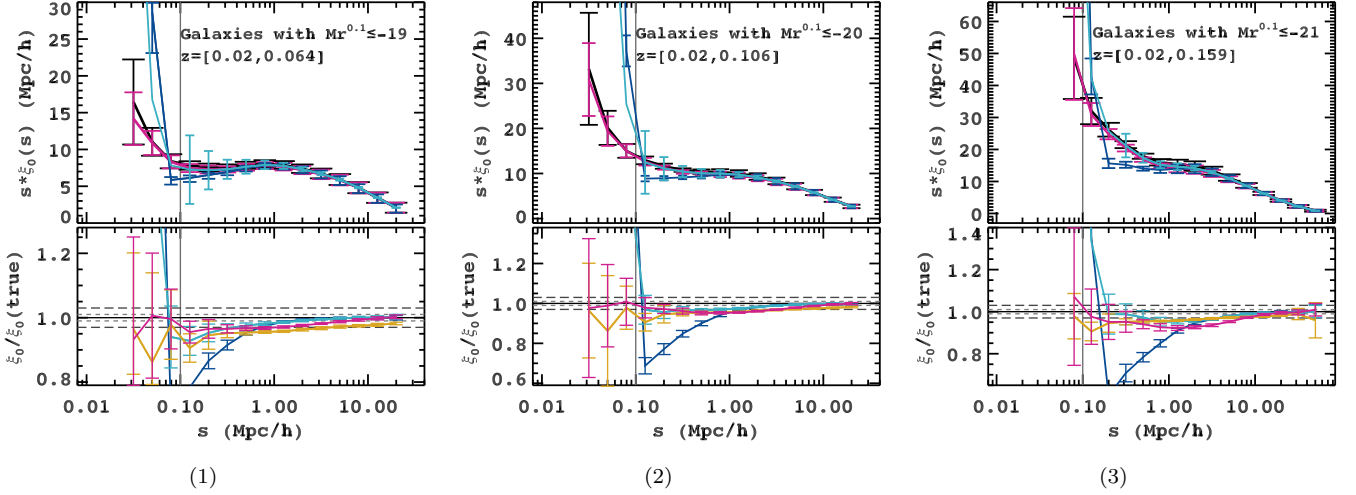


Figure 4. Same as Figure 3 but for the monopole moment  $\xi_0(s)$  of the redshift space correlation functions.

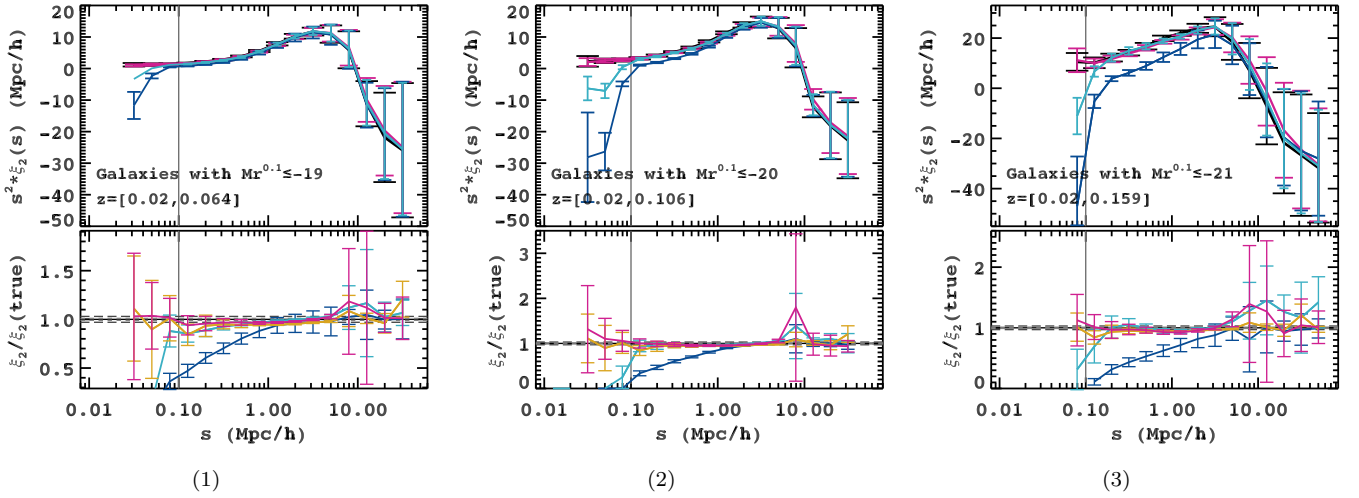


Figure 5. Same as Figure 3 but for the quadrupole moment  $\xi_2(s)$  of the redshift space correlation functions.

such as galaxy clusters, where there tend to be more brighter galaxies than seen in less dense regions (Dressler 1980; Davis & Peebles 1983; Wechsler & Tinker 2018). These luminous galaxies also have a stronger clustering strength than faint galaxies (Zehavi et al. 2005, 2011). In future works, we plan to further consider this dependence on the galaxy luminosity to avoid the limitations arising from the indiscriminate treatments to the different luminous populations.

### 5.2. Differences from Previous Methods

For the NN method, the assumption that each collided galaxy is associated with its nearest neighbor is too strong to recover the true distributions of the fiber-collided populations. This leads to an overclustering bump below the fiber-collision scale, as shown in Figure 3. We argue that the satisfactory agreement on interme-

diated scales of  $w_p(\text{NN})$  is actually a pair compensation effect that only works for  $w_p$ . When it comes to the multipole moments of the correlation functions, the drawbacks are apparent: extremely high biases are shown on small scales and even extending to the intermediate scales, as shown in Figure 4 through 6. These extreme behaviors are directly caused by insufficient modeling of the intrinsic separations of galaxy pairs (Jackson 1972; Peebles 1987; Huchra 1988; Hamilton 1992). More specifically, panel (1) in Figure 2 is modeled by a  $\delta$  function in the case of the NN method. In reality, the line-of-sight separations of the nearest pairs display a Gaussian-like distribution with a higher and broadening wing, as shown in Figure 2. A coherence length around  $20 \text{ Mpc } h^{-1}$  can also be clearly seen (Hahn17). This coherence length is understandable if we recall that a

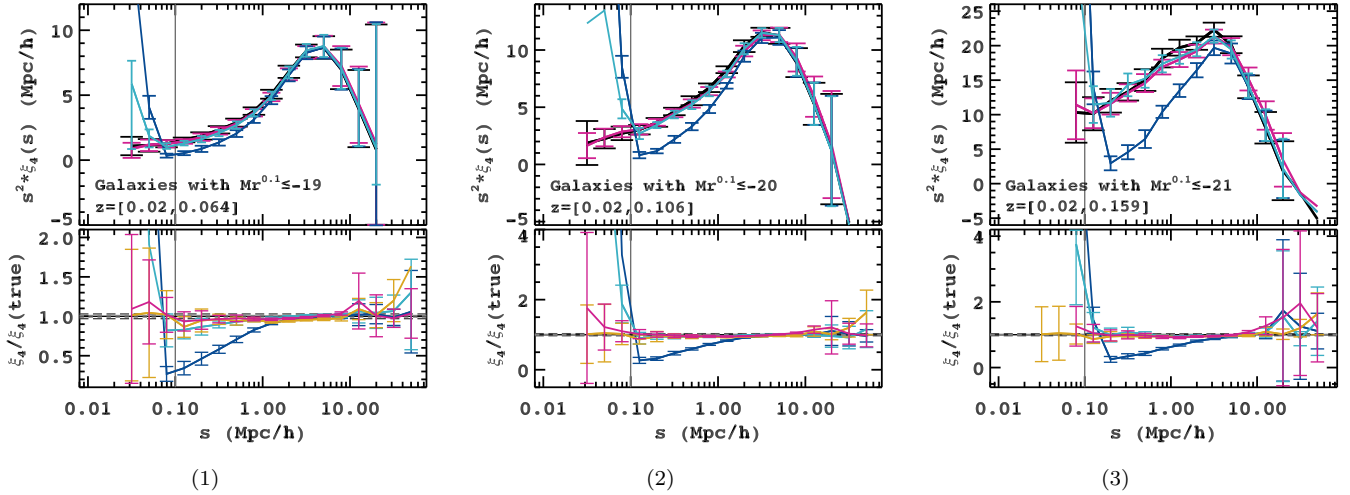


**Figure 6.** Same as Figure 3 but for the hexadecapole moment  $\xi_4(s)$  of the redshift space correlation functions.

typical galaxy coherence length of  $50 \text{ Mpc } h^{-1}$  is measured in the local peculiar velocity field (Peebles 1987). Since the galaxies that are most likely affected by the fiber-collision effect usually reside in dense regions of the universe, where the impact of the peculiar velocities are relatively stronger than those in less dense regions, their coherence length is thus smaller.

To alleviate the problem caused by the intrinsic velocity dispersion of galaxy pairs, Hahn17 conservatively added a Gaussian scatter to the pair displacements for about 70% of pairs within  $3\sigma_{\text{LOS}}$ . The remaining 30% of pairs are kept the same as in the NN method. As expected, the biases of the power spectrum are improved significantly compared with the results of the NN method (see their Figure 3 and Figure 6), despite the correction still being severely limited, especially for the quadrupole power spectrum. In our test of their method, the correlation function appears to have been corrected to a better degree. This might have been caused by many subtle differences between our implementation and their original ones. First of all, we apply the Hahn17 method in real space, while their implementation is in Fourier space. There are also a few differences in the galaxy samples used by our work and theirs. For example, we use the SDSS DR7 “fu111” sample, which covers a smaller volume compared with their BOSS DR12 CMASS sample. The fiber-collision scales are also different for the two SDSS samples. The simulation we adopt to build the mocks has a higher resolution than theirs. So it is not too surprising that the Hahn17 method works well in our tests, which give a slightly better correction results than the NN method. Lastly, we are also aware that one method may give different correction results for the correlation functions in real space and for the power spectrum in Fourier space.

However, further exploring the different performances of a method in different spaces is beyond the scope of this paper.

In the MNN method, first, we adopt a fixed correlation length of  $20 \text{ Mpc } h^{-1}$ , rather than the  $3\sigma_{\text{LOS}}$  scatter applied by Hahn17. Second, two more angular neighbors are taken into account mainly based on the statistical fraction distributions of galaxy pairs from the fiber-collision-free galaxies. Third, in step 2, instead of randomly selecting a galaxy from  $N$  galaxies in the same  $\Delta\theta$  bin of  $\Phi^{01}$ , we introduce a parameter  $N_{\text{near}}$  and we only select a galaxy from  $N_{\text{near}}$  neighbors of the galaxy “ $\tilde{1}$ .” The function of  $N_{\text{near}}$  is to set a range of the possible comoving distances or redshifts. We have tested that a blind and random selection of the  $N$  galaxies in  $\Delta\theta$  bin can result in an underestimation of clustering below the fiber-collision scale. However, the small-scale clustering is not very sensitive to the choice of  $N_{\text{near}}$  as shown in Figure 7. As expected, after these improvements the MNN method effectively lowers the overclustering bump of the two-point correlation functions below the fiber-collision scale. It also presents superior measurements on intermediate scales compared with other methods. For  $w_p$ , the biases are reduced to 1%, and the small deviations are well under the  $1\sigma$  measurement errors. For  $\xi_0$ , although the underestimation is as large as  $\sim 10\%$  as shown in the brightest samples, this underestimation can be partly ascribed to the unmodeled coherent motions of the collided galaxies, a problem that we do not try to resolve in this work.

### 5.3. Choices of Model Parameters

To see the performance of the MNN method if different neighbors and different choices of  $N_{\text{near}}$  are used, we perform further tests, as shown in Figure 7. We try

three different cases: including the fourth neighbor (yellow curves in Figure 7), setting  $N_{\text{near}} = 60$  (light blue curves in Figure 7), and setting  $N_{\text{near}} = 100$  (dark blue curves in Figure 7). We see that only a small bias of  $w_p$  is aroused by using four neighbors below the fiber-collision scale, which is still under the measurement errors as shown. Actually, we have also tried the case of only including two neighbors. This leads to a 3% over-clustering bump of  $w_p$  below the fiber-collision scale, similar to the result from the NN method. Therefore, as supported by the pair fraction statistics in Table 2, the choice of three neighbors gives the best estimation on small scales. On the other hand, the clustering is also not sensitive to the choice of  $N_{\text{near}}$  at all. Even for the multipole moments of the correlation functions, the biases arising from the use of different  $N_{\text{near}}$  in the MNN method are very small.

## 6. SUMMARY

In this paper, we have developed a new method to correct for the fiber-collision effect, which is a common problem in modern spectroscopic galaxy surveys. We mainly focus on correcting galaxy clustering below the fiber-collision scale and the intermediate scale  $\lesssim 10\text{Mpc } h^{-1}$ . The MNN method is basically built upon the previously proposed NN method and the Hahn17 method. The key assumption of this method is that the fiber-collided galaxy is in association with its three nearest angular neighbors. By statistically investigating the line-of-sight comoving separations of the neighboring galaxy pairs with resolved spectroscopic redshifts, we find the association length is  $\sim 20\text{Mpc } h^{-1}$ . To test the method, we use a high resolution  $N$ -body simulation to construct 33 mock galaxy catalogs mimicking the observational selection of the SDSS DR7 “full1” sample from NYU-VAGC. Our main tests of the MNN method are performed with these 33 mocks. By comparing the projected two-point correlation functions and the multipole moments of the correlation functions in real space for three different volume-limited luminosity threshold

samples, we demonstrate that the MNN method can reduce the bias to 1% for  $w_p$ , which is a significant improvement compared with other methods.

The advantages of the MNN method are as follows. First, this method is built upon the intrinsic distribution of galaxy pairs. This distribution is recovered from galaxy pairs within the fiber-collision scale that still have measured redshifts, thanks to overlapping tiling regions in most spectroscopic surveys. Second, a better estimation of the galaxy two-point statistics can be attained below the fiber-collision scale and on the intermediate scale compared with other methods. Third, because the MNN method can assign new redshifts to fiber-collided galaxies and have a good recovery of the true redshift distribution, in principle it can also measure the power spectrum accurately. We will test the performance of our method in Fourier space in our future work. We have also summarized the limitations of the MNN method in Section 5.1, where we believe the coherent motion of galaxy pairs is quite important in the recovery of the redshift-space correlation functions. We are working to improve the MNN method, and will test the improved method with newer data in future works.

## ACKNOWLEDGMENTS

We are grateful to the anonymous referee for insightful suggestions that significantly improved this paper. L.Y. thanks Hong Guo and Zhigang Li and Feng Shi for their useful conversations on mock construction and galaxy clustering measurements. The work is supported by the 973 Program (Nos. 2015CB857002, 2015CB857003) and NSFC (11320101002, 11533006, & 11621303). J.H. is supported by JSPS Grant-in-Aid for Scientific Research JP17K14271. Kavli IPMU is supported by World Premier International Research Center Initiative (WPI), MEXT, Japan.

## REFERENCES

- Alam, S., Albareti, F. D., Allende Prieto, C., et al. 2015, *ApJS*, 219, 12, doi: [10.1088/0067-0049/219/1/12](https://doi.org/10.1088/0067-0049/219/1/12)
- Anderson, L., et al. 2012, *MNRAS*, 427, 3435, doi: [10.1111/j.1365-2966.2012.22066.x](https://doi.org/10.1111/j.1365-2966.2012.22066.x)
- Behroozi, P. S., Conroy, C., & Wechsler, R. H. 2010, *ApJ*, 717, 379, doi: [10.1088/0004-637X/717/1/379](https://doi.org/10.1088/0004-637X/717/1/379)
- Bennett, C. L., Larson, D., Weiland, J. L., et al. 2013, *ApJS*, 208, 20, doi: [10.1088/0067-0049/208/2/20](https://doi.org/10.1088/0067-0049/208/2/20)
- Berlind, A. A., et al. 2006, *ApJS*, 167, 1, doi: [10.1086/508170](https://doi.org/10.1086/508170)
- Beutler, F., Seo, H.-J., Saito, S., et al. 2017, *MNRAS*, 466, 2242, doi: [10.1093/mnras/stw3298](https://doi.org/10.1093/mnras/stw3298)
- Bianchi, D., & Percival, W. J. 2017, *MNRAS*, 472, 1106, doi: [10.1093/mnras/stx2053](https://doi.org/10.1093/mnras/stx2053)
- Bianchi, D., Burden, A., Percival, W. J., et al. 2018, *ArXiv e-prints*. <https://arxiv.org/abs/1805.00951>



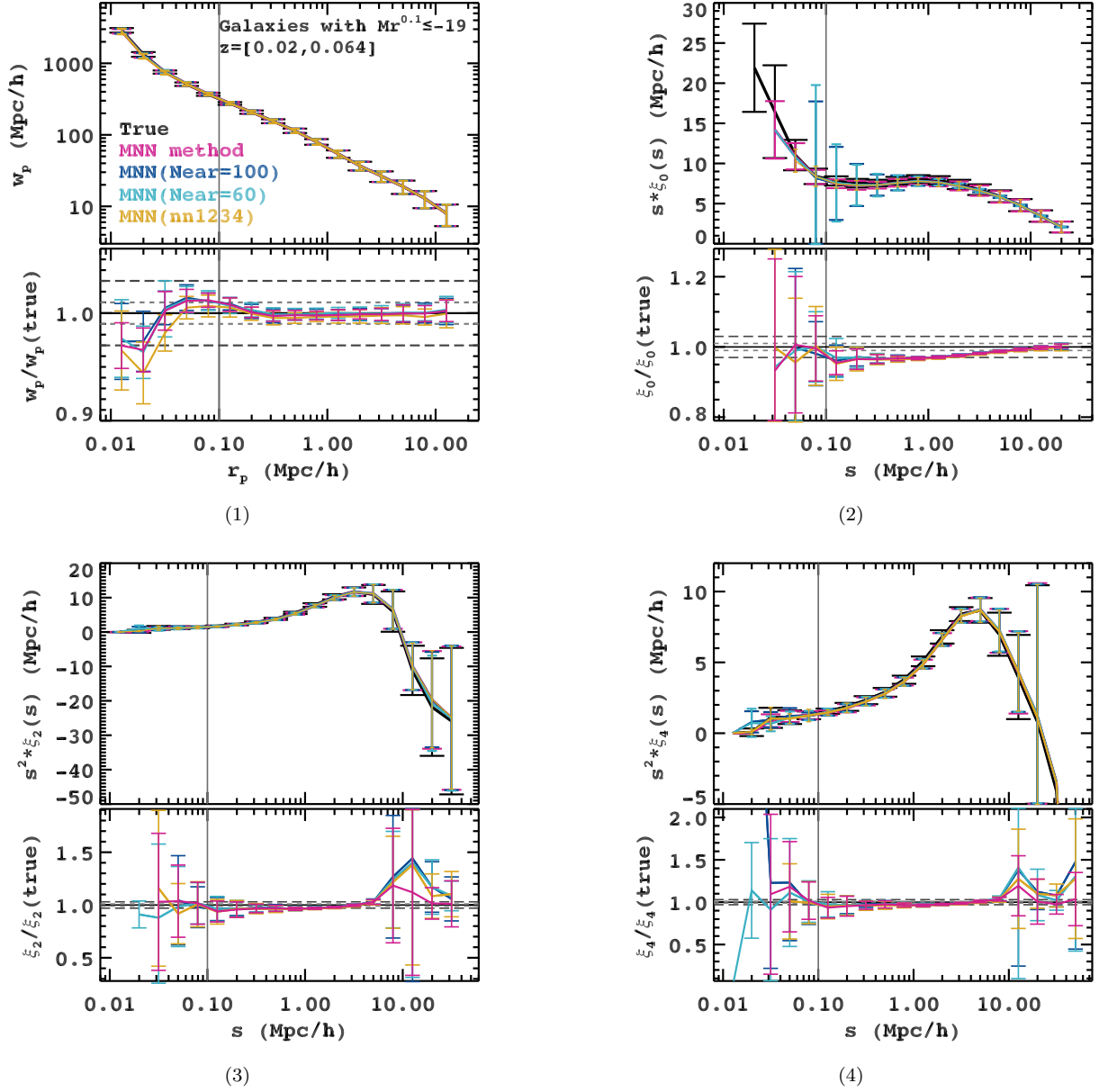


**Figure 7.** Testing the performance of the MNN method with three different choices of parameters: (1) we include four neighbors (yellow) to perform the MNN, instead of three neighbors (magenta); (2) we set  $N_{\text{near}} = 100$  (dark blue) and  $N_{\text{near}} = 60$  (light blue) instead of the first choice of  $N_{\text{near}} = 30$ . Panels (1), (2), (3), and (4) show comparisons of  $w_p$ ,  $\xi_0$ ,  $\xi_2$ , and  $\xi_4$ , respectively. We can see that neither the use of four neighbors nor the choices of  $N_{\text{near}}$  are very sensitive to  $w_p$ ,  $\xi_0$ ,  $\xi_2$ , and  $\xi_4$ . The gray vertical line and the horizontal dotted and dashed lines are the same as in Figure 3.

Blanton, M. R., et al. 2001, *AJ*, 121, 2358,  
doi: [10.1086/320405](https://doi.org/10.1086/320405)

Blanton, M. R., Hogg, D. W., Bahcall, N. A., et al. 2003,  
*ApJ*, 592, 819, doi: [10.1086/375776](https://doi.org/10.1086/375776)

Blanton, M. R., et al. 2005, *AJ*, 129, 2562,  
doi: [10.1086/429803](https://doi.org/10.1086/429803)

Bond, J. R., Kofman, L., & Pogosyan, D. 1996, *Nature*,  
380, 603, doi: [10.1038/380603a0](https://doi.org/10.1038/380603a0)

Cacciato, M., van den Bosch, F. C., More, S., Mo, H., &  
Yang, X. 2013, *MNRAS*, 430, 767,  
doi: [10.1093/mnras/sts525](https://doi.org/10.1093/mnras/sts525)

Cautun, M., van de Weygaert, R., Jones, B. J. T., & Frenk,  
C. S. 2014, *MNRAS*, 441, 2923,  
doi: [10.1093/mnras/stu768](https://doi.org/10.1093/mnras/stu768)

Chaves-Montero, J., Angulo, R. E., Schaye, J., et al. 2016,  
*MNRAS*, 460, 3100, doi: [10.1093/mnras/stw1225](https://doi.org/10.1093/mnras/stw1225)

- Conroy, C., Wechsler, R. H., & Kravtsov, A. V. 2006, *ApJ*, 647, 201, doi: [10.1086/503602](https://doi.org/10.1086/503602)
- Contreras, C., et al. 2013, *MNRAS*, 430, 924, doi: [10.1093/mnras/sts608](https://doi.org/10.1093/mnras/sts608)
- Croton, D. J., Gao, L., & White, S. D. M. 2007, *MNRAS*, 374, 1303, doi: [10.1111/j.1365-2966.2006.11230.x](https://doi.org/10.1111/j.1365-2966.2006.11230.x)
- Dalal, N., White, M., Bond, J. R., & Shirokov, A. 2008, *ApJ*, 687, 12, doi: [10.1086/591512](https://doi.org/10.1086/591512)
- Davis, M., Efstathiou, G., Frenk, C. S., & White, S. D. M. 1985, *ApJ*, 292, 371, doi: [10.1086/163168](https://doi.org/10.1086/163168)
- Davis, M., & Peebles, P. J. E. 1983, *ApJ*, 267, 465, doi: [10.1086/160884](https://doi.org/10.1086/160884)
- Dawson, K. S., Schlegel, D. J., Ahn, C. P., et al. 2013, *AJ*, 145, 10, doi: [10.1088/0004-6256/145/1/10](https://doi.org/10.1088/0004-6256/145/1/10)
- Dawson, K. S., Kneib, J.-P., Percival, W. J., et al. 2016, *AJ*, 151, 44, doi: [10.3847/0004-6256/151/2/44](https://doi.org/10.3847/0004-6256/151/2/44)
- de la Torre, S., et al. 2013, *A&A*, 557, A54, doi: [10.1051/0004-6361/201321463](https://doi.org/10.1051/0004-6361/201321463)
- DESI Collaboration, Aghamousa, A., Aguilar, J., et al. 2016a, *ArXiv e-prints*. <https://arxiv.org/abs/1611.00036>
- . 2016b, *ArXiv e-prints*. <https://arxiv.org/abs/1611.00037>
- Dressler, A. 1980, *ApJ*, 236, 351, doi: [10.1086/157753](https://doi.org/10.1086/157753)
- Eisenstein, D. J., Zehavi, I., Hogg, D. W., et al. 2005, *ApJ*, 633, 560, doi: [10.1086/466512](https://doi.org/10.1086/466512)
- Fisher, K. B., Davis, M., Strauss, M. A., Yahil, A., & Huchra, J. 1994, *MNRAS*, 266, 50
- Gao, L., De Lucia, G., White, S. D. M., & Jenkins, A. 2004, *MNRAS*, 352, L1, doi: [10.1111/j.1365-2966.2004.08098.x](https://doi.org/10.1111/j.1365-2966.2004.08098.x)
- Garilli, B., Paioro, L., Scodeggio, M., et al. 2012, *PASP*, 124, 1232, doi: [10.1086/668681](https://doi.org/10.1086/668681)
- Gil-Marín, H., Percival, W. J., Verde, L., et al. 2017, *MNRAS*, 465, 1757, doi: [10.1093/mnras/stw2679](https://doi.org/10.1093/mnras/stw2679)
- Gunn, J. E., et al. 2006, *AJ*, 131, 2332, doi: [10.1086/500975](https://doi.org/10.1086/500975)
- Guo, H., Zehavi, I., & Zheng, Z. 2012, *ApJ*, 756, 127, doi: [10.1088/0004-637X/756/2/127](https://doi.org/10.1088/0004-637X/756/2/127)
- Guo, H., et al. 2015, *MNRAS*, 453, 4368, doi: [10.1093/mnras/stv1966](https://doi.org/10.1093/mnras/stv1966)
- Guo, H., Zheng, Z., Behroozi, P. S., et al. 2016, *MNRAS*, 459, 3040, doi: [10.1093/mnras/stw845](https://doi.org/10.1093/mnras/stw845)
- Guo, Q., & White, S. 2014, *MNRAS*, 437, 3228, doi: [10.1093/mnras/stt2116](https://doi.org/10.1093/mnras/stt2116)
- Guo, Q., White, S., Li, C., & Boylan-Kolchin, M. 2010, *MNRAS*, 404, 1111, doi: [10.1111/j.1365-2966.2010.16341.x](https://doi.org/10.1111/j.1365-2966.2010.16341.x)
- Guo, Q., White, S., Boylan-Kolchin, M., et al. 2011, *MNRAS*, 413, 101, doi: [10.1111/j.1365-2966.2010.18114.x](https://doi.org/10.1111/j.1365-2966.2010.18114.x)
- Guzzo, L., et al. 2008, *Nature*, 451, 541, doi: [10.1038/nature06555](https://doi.org/10.1038/nature06555)
- Hahn, C., Scoccimarro, R., Blanton, M. R., Tinker, J. L., & Rodríguez-Torres, S. A. 2017, *MNRAS*, 467, 1940, doi: [10.1093/mnras/stx185](https://doi.org/10.1093/mnras/stx185)
- Hamilton, A. J. S. 1992, *ApJL*, 385, L5, doi: [10.1086/186264](https://doi.org/10.1086/186264)
- Han, J., Cole, S., Frenk, C. S., Benitez-Llambay, A., & Helly, J. 2018, *MNRAS*, 474, 604, doi: [10.1093/mnras/stx2792](https://doi.org/10.1093/mnras/stx2792)
- Han, J., Jing, Y. P., Wang, H., & Wang, W. 2012, *MNRAS*, 427, 2437, doi: [10.1111/j.1365-2966.2012.22111.x](https://doi.org/10.1111/j.1365-2966.2012.22111.x)
- Hawkins, E., et al. 2003, *MNRAS*, 346, 78, doi: [10.1046/j.1365-2966.2003.07063.x](https://doi.org/10.1046/j.1365-2966.2003.07063.x)
- Hinshaw, G., Larson, D., Komatsu, E., et al. 2013, *ApJS*, 208, 19, doi: [10.1088/0067-0049/208/2/19](https://doi.org/10.1088/0067-0049/208/2/19)
- Huchra, J. P. 1988, in *Astronomical Society of the Pacific Conference Series*, Vol. 4, *The Extragalactic Distance Scale*, ed. S. van den Bergh & C. J. Pritchet, 257–280
- Jackson, J. C. 1972, *MNRAS*, 156, 1P
- Jiang, C. Y., Jing, Y. P., Faltenbacher, A., Lin, W. P., & Li, C. 2008, *ApJ*, 675, 1095, doi: [10.1086/526412](https://doi.org/10.1086/526412)
- Jing, Y. P. 2018, *ArXiv e-prints*. <https://arxiv.org/abs/1807.06802>
- Jing, Y. P., Börner, G., & Suto, Y. 2002, *ApJ*, 564, 15, doi: [10.1086/324332](https://doi.org/10.1086/324332)
- Jing, Y. P., Zhang, P., Lin, W. P., Gao, L., & Springel, V. 2006, *ApJL*, 640, L119, doi: [10.1086/503547](https://doi.org/10.1086/503547)
- Kaiser, N. 1987, *MNRAS*, 227, 1
- Kennel, M. B. 2004, *ArXiv Physics e-prints*
- Kravtsov, A. V., Berlind, A. A., Wechsler, R. H., et al. 2004, *ApJ*, 609, 35, doi: [10.1086/420959](https://doi.org/10.1086/420959)
- Landy, S. D., & Szalay, A. S. 1993, *ApJ*, 412, 64, doi: [10.1086/172900](https://doi.org/10.1086/172900)
- Levi, M., Bebek, C., Beers, T., et al. 2013, *ArXiv e-prints*. <https://arxiv.org/abs/1308.0847>
- Li, C., Kauffmann, G., Jing, Y. P., et al. 2006, *MNRAS*, 368, 21 (Li06), doi: [10.1111/j.1365-2966.2006.10066.x](https://doi.org/10.1111/j.1365-2966.2006.10066.x)
- Li, Z., Jing, Y. P., Zhang, P., & Cheng, D. 2016, *ApJ*, 833, 287, doi: [10.3847/1538-4357/833/2/287](https://doi.org/10.3847/1538-4357/833/2/287)
- Markwardt, C. B. 2009, in *Astronomical Society of the Pacific Conference Series*, Vol. 411, *Astronomical Data Analysis Software and Systems XVIII*, ed. D. A. Bohlender, D. Durand, & P. Dowler, 251
- Mo, H., van den Bosch, F. C., & White, S. 2010, *Galaxy Formation and Evolution*
- Mohammad, F. G., Granett, B. R., Guzzo, L., et al. 2018, *A&A*, 610, A59, doi: [10.1051/0004-6361/201731685](https://doi.org/10.1051/0004-6361/201731685)
- Peacock, J. A., Cole, S., Norberg, P., et al. 2001, *Nature*, 410, 169
- Peebles, P. J. E. 1987, *Nature*, 327, 210, doi: [10.1038/327210a0](https://doi.org/10.1038/327210a0)

- . 2001, *ApJ*, 557, 495, doi: [10.1086/322254](https://doi.org/10.1086/322254)
- Pinol, L., Cahn, R. N., Hand, N., Seljak, U., & White, M. 2017, *JCAP*, 4, 008, doi: [10.1088/1475-7516/2017/04/008](https://doi.org/10.1088/1475-7516/2017/04/008)
- Piscionere, J. A., Berlind, A. A., McBride, C. K., & Scoccimarro, R. 2015, *ApJ*, 806, 125, doi: [10.1088/0004-637X/806/1/125](https://doi.org/10.1088/0004-637X/806/1/125)
- Reid, B., Ho, S., Padmanabhan, N., et al. 2016, *MNRAS*, 455, 1553, doi: [10.1093/mnras/stv2382](https://doi.org/10.1093/mnras/stv2382)
- Reid, B. A., et al. 2012, *MNRAS*, 426, 2719, doi: [10.1111/j.1365-2966.2012.21779.x](https://doi.org/10.1111/j.1365-2966.2012.21779.x)
- Ross, A. J., et al. 2012, *MNRAS*, 424, 564, doi: [10.1111/j.1365-2966.2012.21235.x](https://doi.org/10.1111/j.1365-2966.2012.21235.x)
- Samushia, L., et al. 2014, *MNRAS*, 439, 3504, doi: [10.1093/mnras/stu197](https://doi.org/10.1093/mnras/stu197)
- Sánchez, A. G., Scóccola, C. G., Ross, A. J., et al. 2012, *MNRAS*, 425, 415, doi: [10.1111/j.1365-2966.2012.21502.x](https://doi.org/10.1111/j.1365-2966.2012.21502.x)
- Sánchez, A. G., Scoccimarro, R., Crocce, M., et al. 2017, *MNRAS*, 464, 1640, doi: [10.1093/mnras/stw2443](https://doi.org/10.1093/mnras/stw2443)
- Scoccimarro, R. 2004, *PhRvD*, 70, 083007, doi: [10.1103/PhysRevD.70.083007](https://doi.org/10.1103/PhysRevD.70.083007)
- Seljak, U., Makarov, A., McDonald, P., et al. 2005, *PhRvD*, 71, 103515, doi: [10.1103/PhysRevD.71.103515](https://doi.org/10.1103/PhysRevD.71.103515)
- Shi, F., Yang, X., Wang, H., et al. 2018, *ApJ*, 861, 137, doi: [10.3847/1538-4357/aacb20](https://doi.org/10.3847/1538-4357/aacb20)
- Simha, V., Weinberg, D. H., Davé, R., et al. 2012, *MNRAS*, 423, 3458, doi: [10.1111/j.1365-2966.2012.21142.x](https://doi.org/10.1111/j.1365-2966.2012.21142.x)
- Springel, V., et al. 2005, *Nature*, 435, 629, doi: [10.1038/nature03597](https://doi.org/10.1038/nature03597)
- Swanson, M. E. C., Tegmark, M., Blanton, M., & Zehavi, I. 2008, *MNRAS*, 385, 1635, doi: [10.1111/j.1365-2966.2008.12948.x](https://doi.org/10.1111/j.1365-2966.2008.12948.x)
- Tegmark, M., Strauss, M. A., Blanton, M. R., et al. 2004, *PhRvD*, 69, 103501, doi: [10.1103/PhysRevD.69.103501](https://doi.org/10.1103/PhysRevD.69.103501)
- Tegmark, M., Eisenstein, D. J., Strauss, M. A., et al. 2006, *PhRvD*, 74, 123507, doi: [10.1103/PhysRevD.74.123507](https://doi.org/10.1103/PhysRevD.74.123507)
- Vale, A., & Ostriker, J. P. 2006, *MNRAS*, 371, 1173, doi: [10.1111/j.1365-2966.2006.10605.x](https://doi.org/10.1111/j.1365-2966.2006.10605.x)
- van den Bosch, F. C., More, S., Cacciato, M., Mo, H., & Yang, X. 2013, *MNRAS*, 430, 725, doi: [10.1093/mnras/sts006](https://doi.org/10.1093/mnras/sts006)
- Wang, H., Mo, H. J., Chen, S., et al. 2018, *ApJ*, 852, 31, doi: [10.3847/1538-4357/aa9e01](https://doi.org/10.3847/1538-4357/aa9e01)
- Wang, L., Weinmann, S. M., De Lucia, G., & Yang, X. 2013, *MNRAS*, 433, 515, doi: [10.1093/mnras/stt743](https://doi.org/10.1093/mnras/stt743)
- Wang, W., Jing, Y. P., Li, C., Okumura, T., & Han, J. 2011, *ApJ*, 734, 88, doi: [10.1088/0004-637X/734/2/88](https://doi.org/10.1088/0004-637X/734/2/88)
- Wang, Y., & Tegmark, M. 2004, *Physical Review Letters*, 92, 241302, doi: [10.1103/PhysRevLett.92.241302](https://doi.org/10.1103/PhysRevLett.92.241302)
- Wang, Y., Zhao, G.-B., Chuang, C.-H., et al. 2017, *ArXiv e-prints*. <https://arxiv.org/abs/1709.05173>
- Watson, D. F., Berlind, A. A., McBride, C. K., & Masjedi, M. 2010, *ApJ*, 709, 115, doi: [10.1088/0004-637X/709/1/115](https://doi.org/10.1088/0004-637X/709/1/115)
- Wechsler, R. H., & Tinker, J. L. 2018, *ArXiv e-prints*. <https://arxiv.org/abs/1804.03097>
- White, M., Blanton, M., Bolton, A., et al. 2011, *ApJ*, 728, 126, doi: [10.1088/0004-637X/728/2/126](https://doi.org/10.1088/0004-637X/728/2/126)
- Yang, X., Mo, H. J., Jing, Y. P., van den Bosch, F. C., & Chu, Y. 2004, *MNRAS*, 350, 1153, doi: [10.1111/j.1365-2966.2004.07744.x](https://doi.org/10.1111/j.1365-2966.2004.07744.x)
- Yang, X., Zhang, Y., Lu, T., et al. 2017, *ApJ*, 848, 60, doi: [10.3847/1538-4357/aa8c7a](https://doi.org/10.3847/1538-4357/aa8c7a)
- Yoon, J. H., Schawinski, K., Sheen, Y.-K., Ree, C. H., & Yi, S. K. 2008, *ApJS*, 176, 414, doi: [10.1086/528958](https://doi.org/10.1086/528958)
- Zehavi, I., et al. 2002, *ApJ*, 571, 172, doi: [10.1086/339893](https://doi.org/10.1086/339893)
- . 2005, *ApJ*, 630, 1, doi: [10.1086/431891](https://doi.org/10.1086/431891)
- . 2011, *ApJ*, 736, 59, doi: [10.1088/0004-637X/736/1/59](https://doi.org/10.1088/0004-637X/736/1/59)
- Zentner, A. R., Hearin, A. P., & van den Bosch, F. C. 2014, *MNRAS*, 443, 3044, doi: [10.1093/mnras/stu1383](https://doi.org/10.1093/mnras/stu1383)